2nd Advanced Optical Metrology Compendium

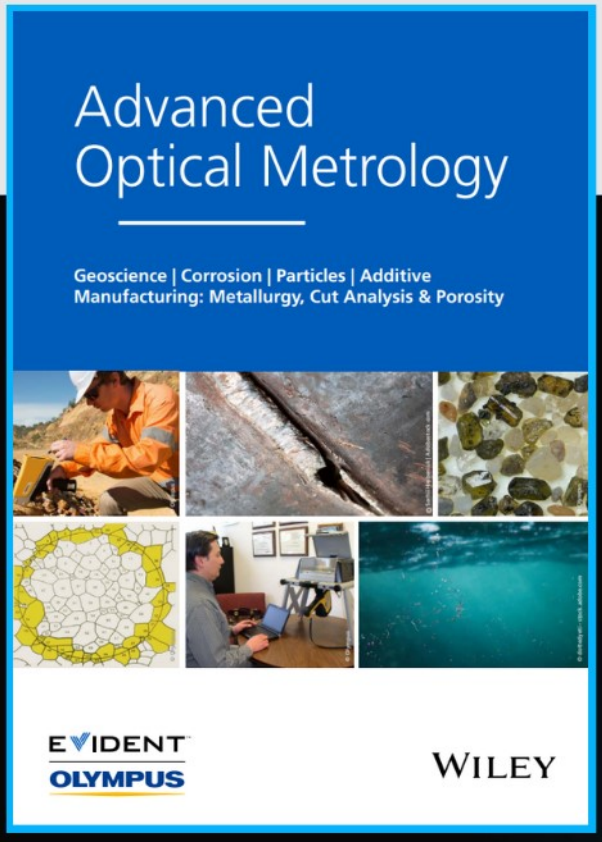

The latest eBook from Advanced Optical Metrology. Download for free.

This compendium includes a collection of optical metrology papers, a repository of teaching materials, and instructions on how to publish scientific achievements.

With the aim of improving communication between fundamental research and industrial applications in the field of optical metrology we have collected and organized existing information and made it more accessible and useful for researchers and practitioners.

EVIDENT
OLYMPUS

WILEY

ADVANCED FUNCTIONAL MATERIALS
www.afm-journal.de

Check for updates

Neuro-Glia-Vascular-on-a-Chip System to Assess Aggravated Neurodegeneration via Brain Endothelial Cells upon Exposure to Diesel Exhaust Particles

Suyeong Seo, Minjeong Jang, Hwieun Kim, Jong Hwan Sung, Nakwon Choi,* Kangwon Lee,* and Hong Nam Kim**

Air pollution induces neurodegeneration, including cognitive deficits, neuroinflammation, and disruption of the blood–brain barrier. The mechanisms underlying air pollution-mediated neurodegeneration have not yet been fully elucidated given the limited knowledge on intercellular interactions. A brain-on-a-chip platform is presented comprising neurons, glia, and brain endothelial cells (bECs; neuro-glia-vascular, NGV) and diesel exhaust particle (DEP)-induced neurodegeneration is evaluated with a particular focus on the intercellular interactions. DEP exposure in the NGV model yields Alzheimer's disease-like signatures, including amyloid beta accumulation, tau phosphorylation, hydrogen peroxide (H_2O_2)/reactive oxygen species (ROS) production, and neuronal cell death. bEC-secreted granulocyte-macrophage colony-stimulating factor (GM-CSF) stimulates microglial activation and the overproduction of H_2O_2/ROS in microglia, suggesting that the bEC-microglia-neuron is a neurodegeneration cascade. Pharmacological inhibition at each step of the cascade, including GM-CSF neutralization, microglial activation suppression, and ROS scavenging, prohibits neurodegeneration in the NGV model. Therefore, intercellular interactions should be further studied of air pollution-induced neurodegeneration.

1. Introduction

Air pollution is a global issue that needs to be solved through industrial development.[1] Recently, the World Health Organization reported that 7 million deaths occur annually as a result of exposure to external and indoor air pollution.[2] Air pollution-related fine particles, termed particulate matter (PM), have a diameter <10 µm and enter the body through the respiratory tract, including the trachea and lungs, during respiration.[3] PM is known to injure the cardiovascular and pulmonary systems, initiating inflammatory responses and oxidative stress.[4,5] Although the toxic effects of PM have mainly been considered in the respiratory and cardiovascular systems,[6] growing evidence has indicated that the brain is also affected by PM. PM invades brain tissue via direct transmission through the nasal

S. Seo, M. Jang, H. Kim, N. Choi, H. N. Kim
Brain Science Institute
Korea Institute of Science and Technology (KIST)
Seoul 02792, Republic of Korea
E-mail: nakwon.choi@kist.re.kr; hongnam.kim@kist.re.kr

S. Seo
Program in Nano Science and Technology
Graduate School of Convergence Science and Technology
Seoul National University
Seoul 08826, Republic of Korea

H. Kim, J. H. Sung
Department of Chemical Engineering
Hongik University
Seoul 04066, Republic of Korea
E-mail: jhsung22@hongik.ac.kr

N. Choi
KU-KIST Graduate School of Converging Science and Technology
Korea University
Seoul 02841, Republic of Korea

The ORCID identification number(s) for the author(s) of this article can be found under https://doi.org/10.1002/adfm.202210123.

© 2022 The Authors. Advanced Functional Materials published by Wiley-VCH GmbH. This is an open access article under the terms of the Creative Commons Attribution License, which permits use, distribution and reproduction in any medium, provided the original work is properly cited.

DOI: 10.1002/adfm.202210123

N. Choi
Division of Bio-Medical Science & Technology
KIST School
Korea University of Science and Technology (UST)
Seoul 02792, Republic of Korea

K. Lee
Department of Applied Bioengineering
Graduate School of Convergence Science and Technology
Seoul National University
Seoul 08826, Republic of Korea
E-mail: kangwonlee@snu.ac.kr

K. Lee
Research Institute for Convergence Science
Seoul National University
Seoul 08826, Republic of Korea

H. N. Kim
School of Mechanical Engineering
Yonsei University
Seoul 03722, Republic of Korea

H. N. Kim
Yonsei-KIST Convergence Research Institute
Yonsei University
Seoul 03722, Republic of Korea

16163028, 0, Downloaded from https://onlinelibrary.wiley.com/doi/10.1002/adfm.202210123 by Seoul National University, Wiley Online Library on [29/12/2022]. See the Terms and Conditions (https://onlinelibrary.wiley.com/terms-and-conditions) on Wiley Online Library for rules of use; OA articles are governed by the applicable Creative Commons License

16163028, 0, Downloaded from https://onlinelibrary.wiley.com/doi/10.1002/adfm.202210123 by Seoul National University, Wiley Online Library on [29/12/2022]. See the Terms and Conditions (https://onlinelibrary.wiley.com/terms-and-conditions) on Wiley Online Library for rules of use; OA articles are governed by the applicable Creative Commons License

epithelium and olfactory receptor neurons [7] or blood circulation.[8] A previous post-mortem study showed that magnetic nanoparticles were observed in the brain tissues obtained from all 38 cases,[9] indicating that PM had penetrated the brain. Individuals exposed to PM show several notable features, such as impaired brain development, cognitive deficits, inflammation in the blood–brain barrier (BBB), and the accumulation of neurotoxic protein aggregates.[8] The exposure of brain tissue to PM has a negative effect on the central nervous system (CNS) and can cause dementia,[10] stroke,[11] depression,[12] and schizophrenia.[13]

To investigate PM toxicity, 2D culture systems and animal models have been widely used. However, these models have several limitations in accurately assessing PM-induced tissue toxicity and its underlying mechanisms.[14] In the 2D culture system, the culture environment loses the 3D extracellular matrix-based architecture and cellular interactions owing to the dissolution of cell-secreted cytokines and limited cell numbers in co-culture.[15,16] The absence of these factors implies a low relevance in vivo, and these dissimilarities make it difficult to accurately predict PM-induced cytotoxic effects. Although animal models yield results that are relevant in vivo, they still possess limitations in terms of genetic heterogeneity, the limited decoupling of cellular and environmental conditions during the experiment, lack of real-time monitoring, and ethical issues.[17,18] They are also costly and require a long experimental period.[19] In previous in vivo studies, animal models have been exposed to aerosols with highly concentrated air pollutants for several weeks or months in specially designed chambers and then sacrificed for further analysis.[20] To overcome the limitations of these models, developments are needed in human tissue-relevant platforms.[21]

Several models have been developed to represent the physiology of human organs to evaluate the toxicity of PM. These models have been primarily based on the respiratory system because fine air pollutants can easily enter the body while breathing and can be deposited in the bronchioles or alveoli.[22] Huh et al. used a lung-on-a-chip device simulating physiological breathing movements to show that in vivo-like cyclic stretching is essential to induce nanoparticle-induced toxicity.[23] Recent studies have further suggested that fine dust also has an adverse effect on brain cells,[6] and 3D human brain models [24,25] have been developed to examine the potential toxic effect of air pollutants on the neurovascular unit. Most brain models have been created by co-culturing brain endothelial cell (bEC)-astrocyte or neuron-astrocyte-microglia in brain-like 3D microenvironments.[26] Cellular responses or dysfunctions have been observed, especially changes in glial cells, such as astrocytes and microglia, upon exposure to PM. Microglia are key regulators of PM-induced toxicity, which is mediated by microglia-generated reactive oxygen species (ROS) upon exposure to PM.[27] Although blood vessels are directly affected by toxic air pollutants, the effects of bECs on PM-induced toxicity have not yet been investigated.

Here, we investigated the effects of bECs on the exacerbation of neurodegeneration using a brain-on-a-chip platform. We engineered a human neuro-glia-vascular (NGV) in vitro system in which the cylindrical vessel is surrounded by neural and glial cells within a 3D hydrogel. We stimulated the brain blood vessels with diesel exhaust particles (DEPs) in the NGV model and examined vascular disorders and cellular responses, including permeability, the production of inflammatory cytokines, oxidative stress, and neuronal function. To decouple the bEC-induced effect, we performed a conditioned media experiment and exogenously added cytokines. The key molecules involved in the aggravation of neurodegeneration, which is closely related to the stimulation of microglia, were identified.

2. Results

2.1. Development of the In Vitro Human NGV Model

Brain tissue exposed to PM shows several pathological signatures including neuronal cell death, neuroinflammation, and blood-brain barrier (BBB) damage.[7] To reflect PM-induced neurotoxic mechanisms (**Figure 1**A), we developed the in vitro human NGV-on-a-chip (Figure S1A, Supporting Information). The endothelium was exposed to gravity-driven perfusion leading to laminar flow with a flow rate of ≈0.1 mm s^{-1}. The medium flow was stopped when the height of the two reservoirs were balanced.[28] Human neural progenitor cells (ReNcell VM), microglia (SV40), and brain microvascular endothelial cells (hBMECs) were cultured in an optimized collagen (Col)/Matrigel (M)/laminin (L) hydrogel contained in the chip (Figure 1A). We optimized the composition of these materials by considering vascular stability and neuronal differentiation (Figure S2, Supporting Information). Col provided structural stability to the gel channel to prevent collapse during the removal of the microneedle. *M* and *L* supported the survival and neuronal differentiation of ReNcell VM and survival of SV40, respectively. Because excessive *M* made the diameter of the gel channel narrower than the microneedle size (235 μm), 30% M was selected (Figure S2A,B, Supporting Information). Neuronal differentiation was promoted upon the addition of *M* and *L* together, compared to Col alone and with *M* only (Col + M), based on the analysis of neuronal marker expression and morphology (Figure S2C–E, Supporting Information). In the Col + M + L condition, the neuronal marker microtubule-associated protein 2 (MAP2) was highly expressed on day in vitro (DIV) 10 (Figure S2C, Supporting Information), and the neuronal morphology changed to include a large number of long branches (Figure S2D,E, Supporting Information), similar to in vivo neurons. The microneedles were used as templates to reconstitute the brain microvasculature. The removal of the microneedles after gelation resulted in the formation of microchannels within the composite hydrogel (Figure S1B, Supporting Information). The brain microvasculature was fabricated by attaching the hBMECs on the luminal side of the microchannel and culturing them. The neurovascular unit (NVU) 3D structures were reconstituted with the brain microvasculature surrounded by neurons, astrocytes, and microglia.

2.2. Characterization of the Engineered Human NGV Model

Prior to investigating DEP-induced toxicity, we characterized an engineered human NGV model using immunofluorescence

© 2022 The Authors. Advanced Functional Materials published by Wiley-VCH GmbH

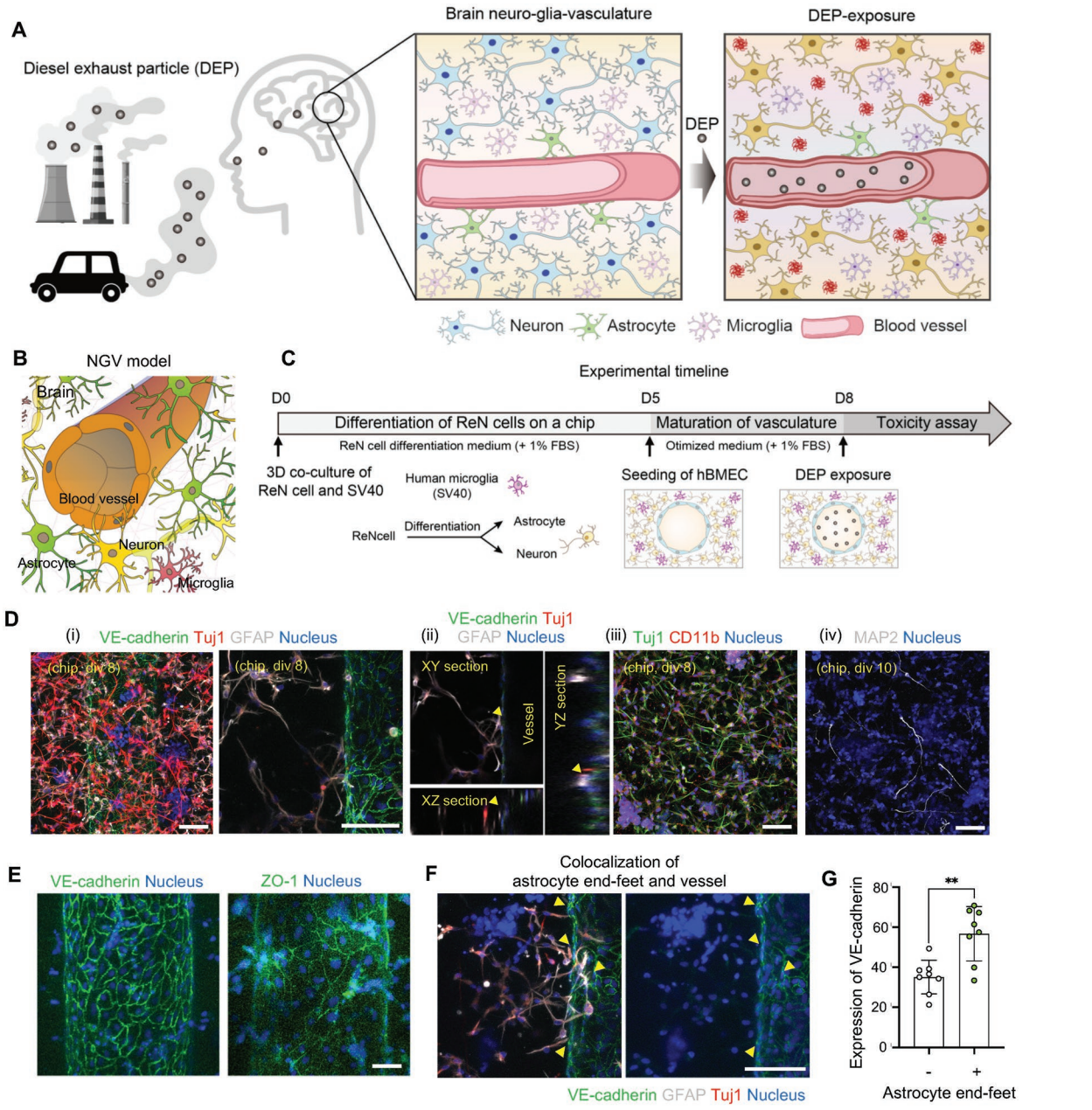

Figure 1. Development of the neuro-glia-vascular (NGV)-on-a-chip. A) Schematic illustration of the effect of diesel exhaust particles (DEPs) on brain neuro-glia-vasculature. B) Schematic illustration of the neurovascularture in the brain. In the cerebrovascular system, there are neurons, astrocytes, and microglia. C) Overall timeline to construct the NGV-on-a-chip. D,E) Immunofluorescent staining of junctional proteins in brain endothelial cells (bECs), VE-cadherin and ZO-1; neuronal markers, Tuj1 and MAP2; astrocyte marker, GFAP; and microglia marker, CD11b, in the NGV-on-a-chip. The nucleus (blue) was counter-stained using DAPI. Scale bars = 100 μm in D and 50 μm in E. F) Co-localization of astrocyte end-feet and brain microvasculature. VE-cadherin (green), GFAP (white), and Tuj1 (red) were stained. The nucleus (blue) was counter-stained using DAPI. Scale bar = 100 μm. G) Expression of VE-cadherin co-localized with (+) and without (-) astrocyte end-feet. The scatter dot plot represents the mean ± standard deviation (SD) with bars and error bars showing all points. Significance was calculated using an unpaired *t*-test ($n = 8$, $^{**}p < 0.01$).

imaging. Neuronal differentiation was confirmed by staining for neuron-specific class III beta-tubulin (Tuj1) and MAP2 (Figure 1D(i),(iv)). Astrocytes expressing glial fibrillary acidic protein (GFAP) spread their end-feet to the endothelium and made direct contact (Figure 1D(ii),(iii)). The microglia (stained with CD11b) co-localized with neurons (Figure 1D(iii)). The expression of tight junctions, zonula occludens-1 (ZO-1), and adherent junctions, vascular endothelial cadherin (VE-cadherin), between adjacent brain endothelial cells was also confirmed (Figure 1E). In the co-localized region of the astrocytic end-feet and endothelium, the expression of junctional proteins (VE-cadherin) increased (Figure 1F,G).

© 2022 The Authors. Advanced Functional Materials published by Wiley-VCH GmbH

16163028, 0, Downloaded from https://onlinelibrary.wiley.com/doi/10.1002/adfm.202210123 by Seoul National University, Wiley Online Library on [29/12/2022]. See the Terms and Conditions (https://onlinelibrary.wiley.com/terms-and-conditions) on Wiley Online Library for rules of use; OA articles are governed by the applicable Creative Commons License

2.3. Characterization of DEPs

We verified the neurotoxicity of PM2.5 (PM with a diameter < 2.5 μm) and DEPs. First, the physiochemical properties of PM2.5 and DEPs were characterized (Figure S3, Supporting Information). According to the scanning electron microscopy results, PM2.5 and DEPs are composed of aggregates of small particles (Figure S3A,B, Supporting Information) in the range of a few tens of nanometers to a few tens of micrometers (Figure S3A,B, Supporting Information). The size distribution of PM2.5 and DEPs ranged from 100–1000 nm. Their average hydrodynamic diameter was approximately 730 nm (Figure S3B, Supporting Information), and they were analyzed using dynamic light scattering (DLS). DEPs have small individual diameters but an aggregated morphology. Nanosized particles can easily penetrate cells and have a relatively large surface area, which makes them highly reactive. The energy dispersive X-ray spectroscopy (EDS) analysis showed that PM2.5 was composed of silicon, potassium, oxygen, aluminum, zirconium, carbon, sodium, and sulfur. Silicon accounted for ≈45% of the entire mass (Figure S3E,G, Supporting Information). By contrast, the DEPs were composed of carbon, oxygen, sulfur, and nitrogen, and carbon accounted for approximately 86% of the whole mass (Figure S3F,H, Supporting Information). The DEPs and PM2.5 had average zeta potential values of −31 and −20 mV, respectively (Figure S3I, Supporting Information). The charge of the particles was one of the factors that affected the interaction between fine particles and cells, including cellular uptake.

2.4. DEP-Induced Toxicity: Vascular Dysfunction and Inflammation

We pre-evaluated the toxicity of PM2.5 and the DEPs and found that the DEPs had higher toxicity in vascular disruption and that the toxic effect of the DEPs was higher than that of PM2.5 (Figure S4, Supporting Information). Furthermore, despite changing the medium three times, vascular integrity was not recovered due to the remaining DEPs on the bECs (Figure S4B, Supporting Information). Based on these observations, we used the DEPs as model PM for further analysis.

Next, we analyzed the effects of DEPs on neurovascular dysfunction (**Figure 2**). When the blood vessels matured (for bECs, DIV 3), the DEP suspension was infused into the endothelium and incubated for 24 h. The medium was then replaced with fresh DEP-free medium, and vascular disruption was observed (Figure 2A). The DEPs significantly induced bEC death after 24 h of exposure (Figure 2B,C, ****,$p < 0.0001$). Western blot and immunofluorescence analyses showed the expression of junctional proteins such as VE-cadherin, platelet endothelial cell adhesion molecules (PECAM-1, also called CD31), ZO-1, and occludin decreased (Figure 2D; Figure S7, Supporting Information), and the expression of intercellular adhesion molecule 1 (ICAM-1), a vascular inflammatory marker, was highly upregulated under DEP-treated conditions (Figure 2D; Figure S7, Supporting Information). Therefore, vascular permeability was significantly increased upon DEP exposure ($P_{control} = 7.487 \times 10^{-8} \pm 1.322 \times 10^{-7}$ cm s^{-1} and $P_{+DEP} = 1.025 \times 10^{-5} \pm 1.031 \times 10^{-5}$ cm s^{-1}; Figure 2E,F). To visualize the disrupted vasculature, we observed the transport of fluorescently labeled nanoparticles by introducing a nanoparticle solution into the brain microvasculature. The nanoparticles showed size-dependent transport across the disrupted vasculature. Small-sized nanoparticles (diameter = 98 nm) were transported through the vasculature when the interstitial flow was applied via hydrostatic pressure difference, while those with a larger size (diameter = 280 nm) did not penetrate the vasculature but accumulated at the surface of the microvasculature (Figure 2G). These results showed that the DEPs induced a small gap in the bECs, suggesting that toxic substances could be transmitted into the brain tissue after the vascular disruption.

We further observed changes in neurons after DEP exposure. In DEP-treated (+) NGV models, the firing rate of calcium signals was elevated with an average value of 2 (F/F_0) in 2 min compared to DEP-untreated (-) conditions (average $F/F_0 = 0.8$; Figure 2H–J). Potassium chloride (KCl) solution (50 mM) was used as a positive control for the stimulated state as KCl is known to increase the firing rate of neurons[29] (Figure 2I). The firing rate in the DEP-exposed case was similar or even higher than that in the KCl-treated case, suggesting the hyperactivity of neurons in response to DEP exposure. Moreover, astrocytes became reactive in the DEP-treated (+) NGV models with an increased expression of gliosis markers, GFAP[30] and vimentin (Figure 2K,M; Figure S7, Supporting Information). Furthermore, the branch length decreased after DEP exposure (Figure 2L). Both neuronal hyperactivity and astrocyte gliosis are considered hallmarks of neurodegenerative disorders such as Alzheimer's disease (AD).[31] These findings suggest that air pollutants are a risk factor for neuronal dysfunction and glia-mediated degeneration.

2.5. Microglia Activated to M1-Like Phenotype by DEP-Induced Vascular Inflammation

Therefore, we hypothesized that the inflammatory response of bECs to DEPs may contribute to the aggravation of neurodegeneration (**Figure 3**A). To verify our hypothesis, we first analyzed the cytokine expression profiles of bECs (Figure 3B; Figure S5A, Supporting Information) and microglia mono- and co-cultured with bECs (Figure 3C; Figure S5B, Supporting Information) in the presence (+) and absence (-) of DEPs. The cytokine expression profiles of bECs changed after DEP treatment, especially the expression of granulocyte-macrophage colony-stimulating factor (GM-CSF), which was highly increased (Figure 3B). Interestingly, the cytokine profile of microglia also changed in the presence (+) and absence (-) of bECs (Figure 3C). In the presence of bECs, the expression of cytokines increased compared to that in the absence of bECs. The expression of GM-CSF was further upregulated by DEP treatment in the presence of bECs. Therefore, we hypothesized that GM-CSF, which is secreted from bECs, is a representative cytokine associated with microglial activation (Figure 3A).

We cultured microglia on NGV chips with only bECs to decouple the influence of other cell types, including neurons and astrocytes. The response of microglia was observed depending on the co-culture with bECs and DEP exposure.

© 2022 The Authors. Advanced Functional Materials published by Wiley-VCH GmbH

16163028, 0, Downloaded from https://onlinelibrary.wiley.com/doi/10.1002/adfm.202210123 by Seoul National University, Wiley Online Library on [29/12/2022]. See the Terms and Conditions (https://onlinelibrary.wiley.com/terms-and-conditions) on Wiley Online Library for rules of use; OA articles are governed by the applicable Creative Commons License

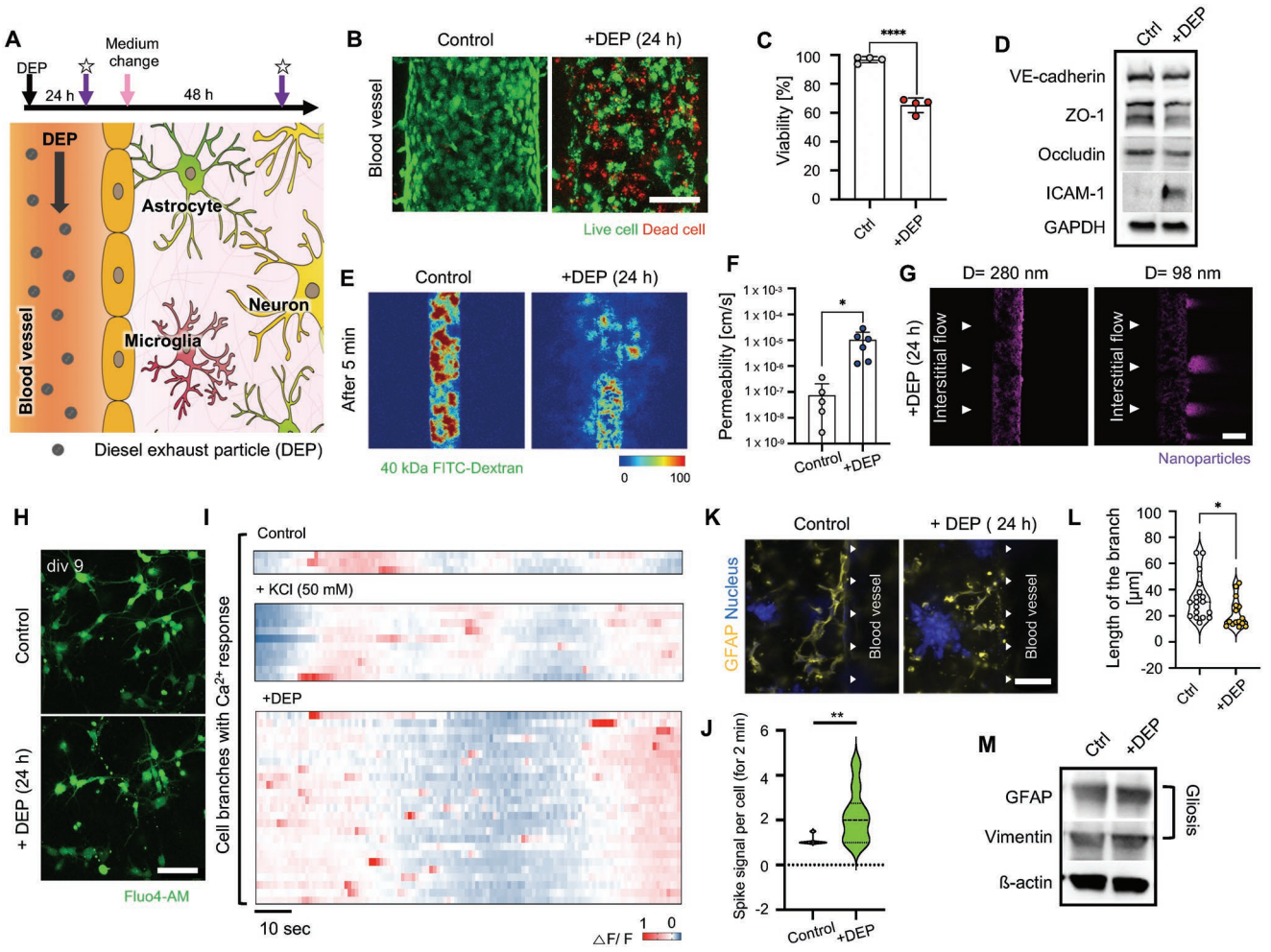

Figure 2. Effect of diesel exhaust particles (DEPs) on the function of brain endothelial cells and neurons. A) Schematics of the overall timeline to study DEP-induced vascular inflammation. B) Live (green) and dead (red) cells represented by Calcein-AM and propidium iodide staining, respectively, after DEP (+DEP) treatment for 24 h, compared to DEP non-treatment (control). Scale bar = 100 µm. C) Viability of the bECs was calculated based on images ($n = 4$, $^{****}p < 0.0001$). D) Expression of junctional proteins, VE-cadherin, ZO-1, and occludin, and inflammatory marker, ICAM-1, under DEP-untreated (-) and -treated (+) conditions. GAPDH was used as a loading control. E) Images of transmitted 40-kDa FITC-dextran through vessels after DEP treatment (+DEP) for 24 h, compared to DEP non-treatment (control). (Scale bar = 200 µm) F) Transendothelial permeability was calculated based on images in E ($n = 5$ in control, $n = 6$ in +DEP, $^{*}p < 0.05$). G) Transport of fluorescently labeled nanoparticles by interstitial flow. (Scale bar = 100 µm) H) Analysis of calcium dynamics using Fluo4-AM (green). (Scale bar = 50 µm) I) Heatmap of calcium signals. F/F_0 was measured and calculated. J) Analysis of spiked calcium signals per cells for 2 min ($n \geq 9$, $^{**}p < 0.01$). K) Analysis of GFAP expression, astrocyte gliosis marker, in the DEP-treated and non-treated NGV model. (Scale bar = 100 µm) L) Length of the branch of astrocyte ($n = 15$–18, $^{*}p < 0.05$). M) Expression of astrocyte gliosis markers, GFAP and vimentin, in the DEP-treated (+) and non-treated control (ctrl) NGV model. ß-actin was used as the loading control. Un-cropped blotting images in D and M are presented in Figure S7 (Supporting Information). The scatter dot plot in C and F represents the mean ± standard deviation (SD) with bars and error bars showing all points. The violin plot in L and J represents the distribution of experimental data. Significance in C, F, L, and J was calculated using an unpaired *t*-test.

In addition, a conditioned medium (CM) from DEP-treated bECs was used to confirm the effect of cytokines secreted from bECs (Figure 3D). Microglial morphology changed into dendritic cell-like morphology with several sprouts and branches (Figure 3E–G) when they were exposed to DEPs. Morphological changes were also observed when the microglia were incubated with CM collected from DEP-treated bECs or when they were exposed to DEPs in co-culture conditions with bECs (Figure 3E–G). However, in the absence of bECs, the exposure of microglia to DEPs did not cause remarkable changes in cell morphology (Figure 3E–G). The expression of microglia activation and M1 polarization markers,[32] including CD11b, CD68, and CD40, increased following DEP exposure (+) with bEC co-culture conditions and bEC-CM treatment conditions compared to non-treatment (-) cases (Figure 3H; Figure S7, Supporting Information). The results showed that the bEC-secreted factors that were produced upon DEP exposure stimulated microglial activation.

To specify the cytokine secreted from bECs to activate microglia, GM-CSF was targeted as it was highly increased in bECs upon DEP exposure and is known to be related to microglial activation (Figure 3B,C). GM-CSF was exogenously treated

© 2022 The Authors. Advanced Functional Materials published by Wiley-VCH GmbH

16163028, 0, Downloaded from https://onlinelibrary.wiley.com/doi/10.1002/adfm.202210123 by Seoul National University, Wiley Online Library on [29/12/2022]. See the Terms and Conditions (https://onlinelibrary.wiley.com/terms-and-conditions) on Wiley Online Library for rules of use; OA articles are governed by the applicable Creative Commons License

16163028, 0, Downloaded from https://onlinelibrary.wiley.com/doi/10.1002/adfm.202210123 by Seoul National University, Wiley Online Library on [29/12/2022]. See the Terms and Conditions (https://onlinelibrary.wiley.com/terms-and-conditions) on Wiley Online Library for rules of use; OA articles are governed by the applicable Creative Commons License

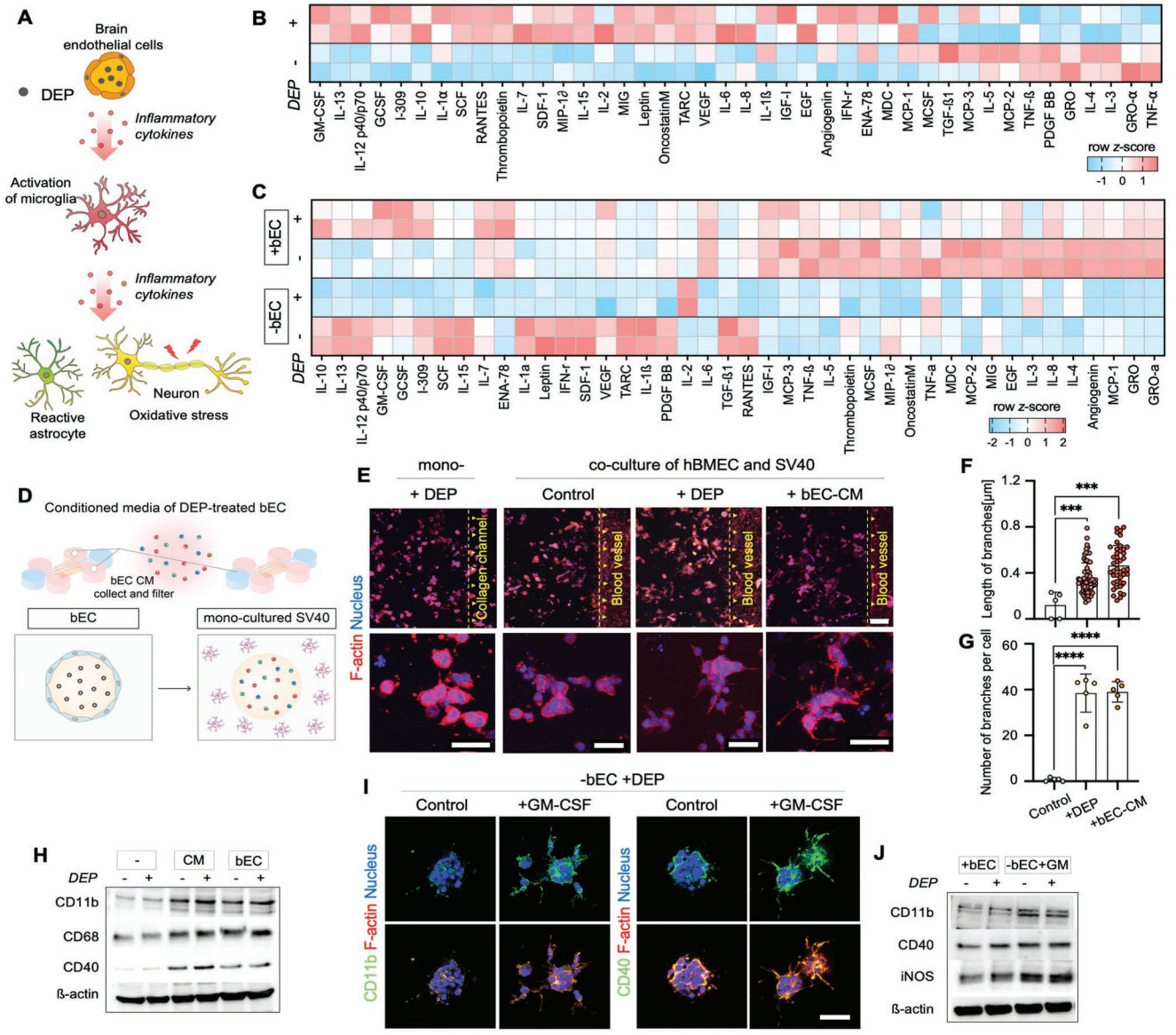

Figure 3. bEC-secreted inflammatory cytokines induced microglia activation. A) Proposed mechanism of inflammatory cytokine-induced neurotoxicity by DEP treatment. B,C) Analysis of inflammatory cytokines secreted from bECs (B) and microglia mono- (-bEC) and co-cultured with bECs (+bEC) (C) in the presence (+) and absence (-) of DEP. Heatmap represented by the z-score in ascending order when treated with DEP compared to non-treatment. D) Schematic illustration of the co-cultured system of microglia and bECs. To analyze the effect of bEC-secreted inflammatory cytokines on microglial activation, conditioned media from DEP-treated bECs (bEC-CM) were collected and treated in a microglia mono-cultured system. E–G) Morphological analysis of microglia when bECs were co-cultured with DEPs (+DEP) and compared to conditioned media (CM) obtained from the DEP-treated bECs (bEC-CM) [scale bar = 100 μm (top images), 50 μm (bottom images)]. The morphology of microglia was visualized by F-actin (red) and nucleus (blue) staining (E). Based on the image analysis, the length (F) and number (G) of branches were calculated ($n \geq 5$ in F, $n = 5$ in G, $^{***}p < 0.001$, $^{****}p < 0.0001$). H) Expression of microglial activation markers, CD11b, CD68, and CD40, under CM and bECs co-cultured (bEC) conditions without (-) / with (+) DEP exposure. β-actin was used as the loading control. I,J) Effects of GM-CSF on microglial activation. GM-CSF was exogenously added to a microglia mono-cultured system without bECs (-EC+GM) to compare the morphology and marker expression of microglia in the presence of bEC (+EC) with (+) and without (-) DEP treatment. I) Immunofluorescence staining of CD11b, CD40 and F-actin in +bEC and -bEC+GM conditions. The nucleus (blue) was counter-stained using DAPI. (Scale bar = 100 μm) J) Expression of CD11b, CD40, and iNOS in +EC and -EC+GM conditions. β-actin was used as the loading control. Un-cropped blotting images in H and J are presented in Figure S7 (Supporting Information). The scatter dot plot in F and G represents the mean ± standard deviation (SD) with bars and error bars showing all points. Significance in F and G was calculated using an ordinary one-way ANOVA Tukey's multiple comparisons test.

in a microglia mono-culture system, and the morphology and microglial marker expression were compared to those in the bEC co-culture system (Figure 3I,J; Figure S7, Supporting Information). The expression of microglial activation markers,[32] including CD11b, CD40, and inducible nitric oxide synthase (iNOS), increased in the GM-CSF-treated cells, even in the microglia mono-cultured system (Figure 3I,J; Figure S7, Supporting Information). The exogenous addition of GM-CSF

© 2022 The Authors. Advanced Functional Materials published by Wiley-VCH GmbH

16163028, 0, Downloaded from https://onlinelibrary.wiley.com/doi/10.1002/adfm.202210123 by Seoul National University, Wiley Online Library on [29/12/2022]. See the Terms and Conditions (https://onlinelibrary.wiley.com/terms-and-conditions) on Wiley Online Library for rules of use; OA articles are governed by the applicable Creative Commons License

resulted in similar microglial activation, even in the absence of DEP exposure (Figure 3J; Figure S7, Supporting Information). Based on these results, it was confirmed that cytokines released from DEP-exposed bECs, especially GM-CSF, are important for microglial activation and M1 polarization.

2.6. M1 Polarization of Microglia Induced Neurotoxicity and Neurodegeneration

We evaluated whether activated microglia caused neurodegeneration in NGV models by comparing neurodegeneration depending on the presence or absence of microglia in synergy with the contribution of bECs (**Figure 4**A,B). When the DEPs or EC-CM were applied to the NGV chip, the viability of neuronal cells decreased. This decrease was more severe in the EC-CM-treated group. The inflammatory cytokine GM-CSF, therefore, aggravates neurodegeneration via excessive microglial activation. In the absence of microglia, however, cell viability remained constant (Figure 4C,D). We also analyzed the inflammatory cytokines in the media of the NGV chip. The production of interleukin (IL)-6 and -8 was elevated under DEP-treated conditions in the presence but not absence of microglia (Figure 4E), indicating that the neurotoxic effect was accelerated by activated microglia stimulated by bECs directly exposed to DEPs. The production of IL-6 and -8, which are involved in neuroinflammation and neurotoxic potential, was considerably upregulated.

DEP exposure is known to induce vascular inflammation, microglial activation-induced neurotoxicity, and further neurodegeneration.[33–35] In our DEP-treated NGV model, the neurodegenerative process was observed, with a particular focus on the signatures of AD-like pathologsies. Amyloid-beta (Aβ) was overexpressed and tau was abnormally hyperphosphorylated in DEP-treated NGV models in the co-presence of bECs and microglia or the co-presence of microglia and bEC-CM (Figure 4F,G; Figures S6, and S7, Supporting Information). Additionally, the presence of tau protein clumps, which are abnormal protein aggregates, was more evident in the axonal region of neurons in the DEP-treated NGV models (Figure 4H,I).

The production and accumulation of H_2O_2 increased in response to DEPs in the culture medium and cell lysates from the DEP-treated (+) NGV models (Figure 4J). The overproduction of H_2O_2 is known to be related to the progression of AD.[36] Protein oxidation due to oxidative stress was also observed at the carbonyl groups in the protein side chain in the DEP-treated (+) NGV models (Figure 4K). The production of reactive oxygen species (ROS) in neuronal cells was further observed in the DEP-treated NGV models (Figure 4L,M). A western blot analysis showed an increased expression of nuclear factor kappa-light-chain-enhancer of activated B cells (NF-κB) and iNOS (Figure 4N; Figure S7, Supporting Information). NF-κB increased greatly under DEP-treated conditions, suggesting the activation of inflammatory signaling pathways (Figure 4O; Figure S7, Supporting Information). ROS production can result from inflammation and NF-κB activation via iNOS expression.[32,37] Overall, the presence of bEC-secreted factors in synergy with microglia induced AD-like phenotypes, including increased H_2O_2/ROS production, accumulation of Aβ and phosphorylated tau, and activated NF-κB signaling pathways.

2.7. Therapeutic Approaches for Air Pollutant-Induced Neurotoxicity

Based on our results and those of previous studies, we found that microglial activation is a key factor in neuronal cell death. Microglial activation can be upregulated by GM-CSF produced by DEP-exposed bECs. Therefore, we evaluated the possibility of suppressing DEP-induced neurodegeneration using three approaches: i) the neutralization of GM-CSF using an antibody, ii) suppression of microglial activation using drugs, and iii) neutralization of ROS by scavenger drugs (**Figure 5**A).

First, we focused on GM-CSF, which is a microglial activation-induced cytokine secreted from bECs (Figure 5B–D). Antibodies against GM-CSF (GM-CSF Ab) were used to neutralize the activity of GM-CSF, and we examined whether exogenous GM-CSF treatment induced neurodegeneration. Indeed, the exogenous addition of GM-CSF induced Aβ accumulation and tau phosphorylation on the NGV chip (Figure 5B,C) with decreased cellular viability (Figure 5D), even in untreated conditions. The addition of antibodies suppressed Aβ accumulation, tau phosphorylation, and neurodegenerative processes, as confirmed by immunofluorescence staining, western blotting, and viability tests (Figure 5B–D). Second, we directly inhibited microglial activation using the well-known microglia inhibitors, pioglitazone[38,39] and minocycline[40] (Figure 5E,F). The inhibition of microglial activation increased cell viability, similar to that observed in the control group. Finally, the scavenging of ROS by astaxanthin[41] also rescued cellular viability (Figure 5E,F).

These results indicate that DEP-exposed bECs stimulate microglial activation and polarization to the M1 phenotype, subsequently resulting in neurotoxicity. Such neurodegenerative cascades can be inhibited by intervening at each step, such as GM-CSF neutralization, microglial activation, and ROS scavenging. Given these findings, environmental toxicity should be considered in the context of cell–cell and cell–microenvironment interactions rather than cell type-specific responses.

3. Discussion

In this study, we engineered an NGV in vitro system to investigate the effect of bECs on the exacerbation cascade of neurodegeneration. The engineered NGV system comprised a cylindrical vessel surrounded by neural and glial cells within a 3D hydrogel. To examine the effect of air pollution on neurodegeneration, we stimulated the brain blood vessels with DEP in the NGV model and examined the induced cellular and microenvironmental changes, including vascular and neuronal disfunction, as well as the production of inflammatory cytokines and oxidative stress. Since our human brain cell-based organ-on-a-chip has brain microvasculature-like structures, the disruption of the functional barrier characteristics could be examined via fluorescence imaging. Furthermore, collection of cell culture media and cells enabled the biological analysis of cellular and microenvironmental changes, such as cytokine production and protein-level changes.

Our study shows that recapitulating brain physiology in vivo, in particular intercellular interactions, is indispensable

© 2022 The Authors. Advanced Functional Materials published by Wiley-VCH GmbH

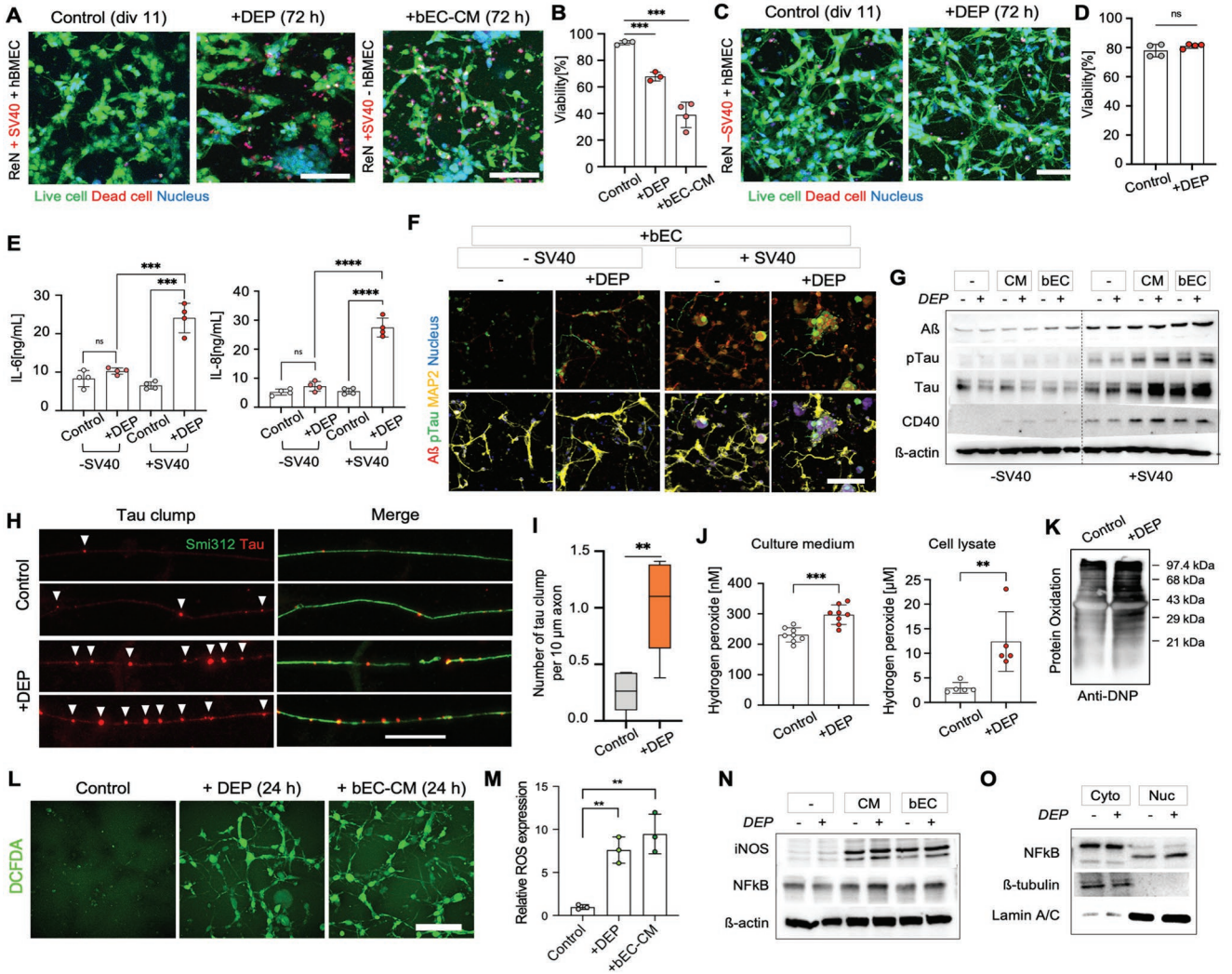

Figure 4. DEP-induced microglial activation regulates neurotoxic effects. A–D) Viable cells were visualized (A and C) and quantified (B and D). Live (green) and dead (red) cells were stained by Calcein-AM and PI, respectively. The nucleus (blue) was counter-stained using Hoechst 33 342. (Scale bar = 100 µm) A,B) In the presence of microglia, the DEPs induced neurotoxicity and decreased viability. Similar toxicity was also observed in the treatment of CM from DEP-exposed endothelial cells. C,D) However, in the absence of microglia, the DEPs did not induce cytotoxicity. (n = 3–4 in B, n = 4 in D, ***$p < 0.001$ and ns; no significance) E) Production of IL-6 and -8 in the NGV models co-cultured with endothelial cells (bEC) and incubated with CM from bEC (bEC-CM) under DEP-treated condition (n = 4, ***$p < 0.001$ and ****$p < 0.0001$) F) Expression of Aβ (red) and phosphorylated tau (pTau, green) in DEP-treated NGV models in the presence of bECs and microglia (SV40), MAP2 (yellow) and nucleus (blue) were counter-stained (Scale bar = 100 µm). G) Western blot analysis of Aβ, tau, pTau, and CD40 levels in DEP-treated and/or non-treated NGV models in the presence (+) and/or absence (-) of bECs (EC) and microglia (SV40). β-actin was used as a loading control. H) Immunofluorescence analysis of tau clumps (red, white marks) in DEP-treated NGV models. Smi312 (green) was counter-stained. (Scale bar = 20 µm) I) Quantified number of tau clumps per 10 µm of the axon ($n > 5$, **$p < 0.01$). J) The production of hydrogen peroxide (H_2O_2) in the CM (left, n = 8) and cell lysates (right, n = 5) from DEP-treated (+) and untreated (control) NGV models. **$p < 0.01$, ***$p < 0.001$. K) Protein oxidation in DEP-treated (+) and untreated (control) NGV models. L) Analysis of reactive oxygen species (ROS) production in neuronal cells under bECs (EC) co-cultured and CM of bEC treated conditions with DEP exposure by 2′,7′-dichlorofluorescein diacetate (DCFDA) staining. (Scale bar = 50 µm) M) The relative ROS expression under bECs co-cultured and CM of bEC-treated conditions with DEP exposure ($n > 3$, ****;$p < 0.0001$) N) Expression of iNOS and NF-κB in microglia under bECs (EC) co-cultured and CM of bEC treated condition with (+) or without (-) DEP exposure. β-actin was used as a loading control. O) Analysis of cytoplasmic and nuclear NF-κB in microglia under bECs co-cultured condition with (+) or without (-) DEP exposure. β-tubulin and lamin A/C were used as loading controls for cytoplasmic and nuclear proteins, respectively. Un-cropped blotting images in G, N, and O are presented in Figure S7 (Supporting Information). The scatter dot plot in B, D, E, J, and M represents the mean ± standard deviation (SD) with bars and error bars showing all points. Significance in D and J was calculated using an unpaired t-test. Significance in B, E, and M was calculated using an ordinary one-way ANOVA Tukey's multiple comparisons test.

for the accurate assessment of neurotoxicity caused by hazardous air pollutants. The contribution of microglia to PM-induced neurodegeneration has been previously described.[24–26] Multiple studies have confirmed the mechanisms by which microglia-generated ROS kill neurons under microglia co-culture conditions.[24–26] Indeed, when neurons are cultured alone, PM exposure does not induce neuronal cell death, whereas neuronal cell death upon PM exposure

© 2022 The Authors. Advanced Functional Materials published by Wiley-VCH GmbH

16163028, 0, Downloaded from https://onlinelibrary.wiley.com/doi/10.1002/adfm.202210123 by Seoul National University, Wiley Online Library on [29/12/2022]. See the Terms and Conditions (https://onlinelibrary.wiley.com/terms-and-conditions) on Wiley Online Library for rules of use; OA articles are governed by the applicable Creative Commons License

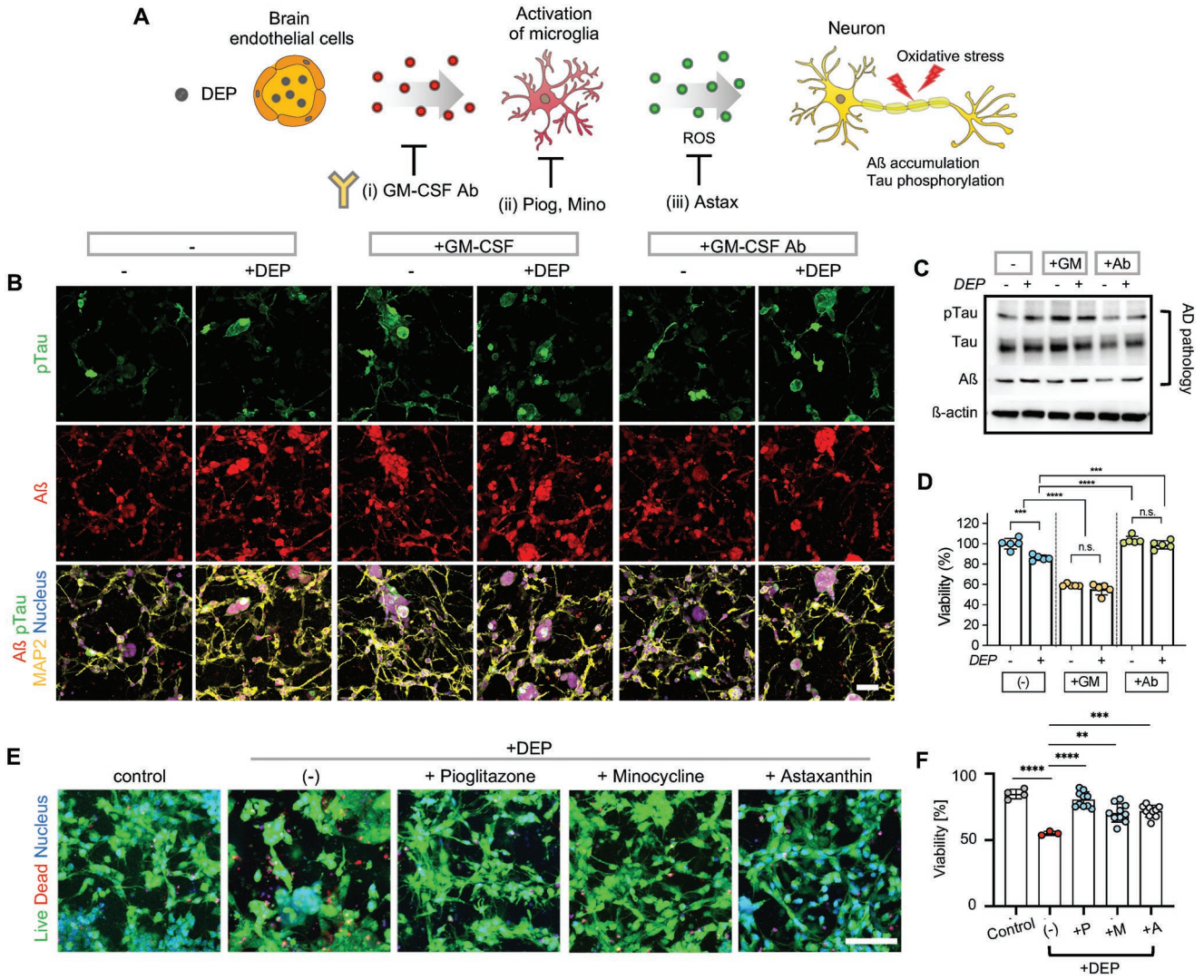

Figure 5. Targeting microglial activation to attenuate neurodegeneration. A) Schematic illustration of the neurodegeneration cascade based on the bEC-microglia-neuron interaction. Therapeutic approaches to inhibit the neurodegeneration cascade via i) direct neutralization of GM-CSF by the antibody (Ab), ii) direct inhibition of microglial activation by the inhibitors, pioglitazone (Piog) and minocycline (Mino), and iii) scavenging of ROS by using astaxanthin (Astax). B–D) Effect of GM-CSF neutralization on the inhibition of neurodegeneration. GM-CSF and its antibody (GM-CSF Ab) were exogenously applied to the NGV chip with (+) and without (-) DEP exposure. B) Immunofluorescence staining of Aβ (red) and pTau (green) on the NGV chip with (+) and without (-) DEP exposure after treatment with GM-CSF and its antibody (GM-CSF Ab). MAP2 (yellow) and nucleus (blue, DAPI) were counter-stained. Scale bar = 50 µm. C) Expression of Aβ, tau, and pTau on the NGV chip with (+) and without (-) DEP exposure by treating GM-CSF (+GM) and its antibody (+ Ab). β-actin was used as the loading control. D) Cell viability on the NGV chip with (+) and without (-) DEP exposure after treatment with GM-CSF (+GM) and its antibody (+ Ab) ($n = 5$, $^{****}p < 0.0001$, n.s.; no significance). E,F) Cell viability after pioglitazone, minocycline, and astaxanthin treatment on the DEP-treated NGV chip. Live (green) and dead (red) cells were stained by Calcein-AM and PI, respectively. The nucleus (blue) was counter-stained using Hoechst 33 342. (Scale bar = 100 µm) F) Quantification of cell viability based on the image analysis ($n = 3$–10, $^{**}p < 0.01$, $^{***}p < 0.001$, $^{****}p < 0.0001$). Un-cropped blotting images in C are presented in Figure S7 (Supporting Information). The scatter dot plot in D and F represents the mean ± standard deviation (SD) with bars and error bars showing all points. Significance in D and F was calculated using an ordinary one-way ANOVA Tukey's multiple comparisons test.

is induced in the presence of microglia. However, to date, the contribution of bECs remains unclear. To the best of our knowledge, this is the first study to demonstrate that bECs can aggravate DEP-induced neurodegeneration by stimulating microglia. To decouple the bEC-induced effect, we performed a conditioned media experiment and found that the key factor underlying bEC-induced microglial stimulation was GM-CSF.

GM-CSF, which is produced by several cell types, including bECs, has a unique role in the activation of microglia and affects neuronal function.[42] In our NGV system, DEP-induced vascular inflammation exacerbated the cytokine storm with elevated GM-CSF levels, and concomitant microglia activation and phenotypical changes to M1. Exogenous addition of GM-CSF also promoted microglia activation; hence, we concluded that bEC-released cytokines are important for microglia activation

© 2022 The Authors. Advanced Functional Materials published by Wiley-VCH GmbH

16163028, 0, Downloaded from https://onlinelibrary.wiley.com/doi/10.1002/adfm.202210123 by Seoul National University, Wiley Online Library on [29/12/2022]. See the Terms and Conditions (https://onlinelibrary.wiley.com/terms-and-conditions) on Wiley Online Library for rules of use; OA articles are governed by the applicable Creative Commons License

16163028, 0, Downloaded from https://onlinelibrary.wiley.com/doi/10.1002/adfm.202210123 by Seoul National University, Wiley Online Library on [29/12/2022]. See the Terms and Conditions (https://onlinelibrary.wiley.com/terms-and-conditions) on Wiley Online Library for rules of use; OA articles are governed by the applicable Creative Commons License

and further neuronal dysfunction. Considering that the clinical signatures of BBB disruption are also noticeable in PM-exposed brain tissue, the contribution of bECs should also be considered in air pollution-induced neurodegeneration.

Our findings indicate that the cell-cell and cell-microenvironmental interaction should be considered in the study of air pollutant-induced neurodegeneration. As shown in the i) DEP-induced stimulation of EC, ii) bEC-secreted GM-CSF-induced microglial activation, and iii) excessive production of ROS by activated microglia, the pathological progression is mediated by multistep cascade. However, animal models possess inherent limitations in addressing such complex cascade due to the following reasons; they only allow end-point assay and they are unable to decouple cellular and microenvironmental factors. The microphysiological systems resolve such unmet needs by allowing real-time observation under a microscope and controlling cellular composition and microenvironment. Therefore, the unknown mechanism in environmental toxicology can be identified by using human cell-based microphysiological systems.

In our DEP-exposed NGV system, neuron and glia cells represent the neurotoxic and neuroinflammatory responses, including neuronal hyperactivity and gliosis of astrocytes, which are hallmarks of neurodegenerative disorder.[31] Astrocytes are key regulators of the inflammatory response in the brain.[30] In AD, the number of reactive astrocytes increases with increased H_2O_2 production and oxidative stress, an event that is correlated with AD pathology.[30,36,43,44] Also, pericytes control the contraction of capillaries in human AD brain, which can evoke the ROS production.[45] Pericyte loss can influence AD-like neurodegeneration with elevation of brain Aß production in mice by overexpressing Aß-precursor protein,[46] and further induce amyloid angiopathy and cerebral ß-amyloidosis by collapsing Aß clearance system. Impaired Aß clearance mechanism also induces excess Aß deposit and disease onset in brain[47,48] However, in this study, we primarily focused on the bEC–microglia interaction. Considering that stimulated bECs secrete various inflammatory cytokines, there is a possibility that those inflammatory cytokines may stimulate astrocytes as well; thus, further studies are needed to investigate the contribution of astrocytes to the DEP-induced neurodegeneration. Furthermore, it is necessary to study DEP-induced neurovascular disease, focusing on the crosstalk between pericyte and BBB. In addition, it is also needed to consider an Aß clearance system to recapitulate a more in vivo-like NGV model.

4. Conclusion

In summary, we identified PM-induced neurodegeneration using a human cell-based brain-on-a-chip platform. GM-CSF-induced changes were confirmed through the exogenous addition of GM-CSF or antibody-mediated neutralization. The DEP-bEC-microglia cascade was closely related to the pathological phenotypes of AD, such as Aβ accumulation, tau phosphorylation, H_2O_2/ROS production, and neuronal cell death. Collectively, these results indicate that assessing cellular interactions is important in studying environmental toxicity. Noteworthily, our NGV platform may represent a valuable tool to investigate the neurotoxic mechanisms underlying the toxic effects of air pollutants in brain disorders and assessing targeted therapeutics for air pollution-related environmental toxicity.

5. Experimental Section

Experimental Design: A brain-on-a-chip (NGV model) was developed in which four types of human brain cells were cocultured. Analysis of the cytokine profile of the NGV model suggested that the bEC-secreted GM-CSF could be a key molecule to stimulate microglia. This hypothesis was evaluated by exogenously adding GM-CSF or supplying bEC-conditioned media in the NGV model. The consequent cell-level changes were evaluated by measuring permeability, viability, ROS expression, immunofluorescence imaging, and western blot analysis, and the microenvironment-level changes were evaluated by cytokine assays. Pharmacological inhibition studies were also performed to evaluate whether the bEC-induced accelerated neurodegeneration could be prevented. Three points of the bEC-induced neurodegeneration cascade, including GM-CSF secretion, microglial activation, and ROS production, were targeted using specific antibodies and drugs.

Fabrication of the Microfluidic Device: To fabricate polydimethylsiloxane (PDMS) microfluidic devices, Sylgard 184 PDMS (SYLGARD 184 Silicone Elastomer; Dowhitech Co., Gyeonggi, South Korea) was mixed with a curing agent at a weight ratio of 10:1 and poured into a mold containing microneedles (diameter = 235 µm) to generate a hollow channel. After polymerizing the PDMS for 3 h at 80 °C, the microneedles were pulled from the cured PDMS and punched with a rectangular hole (4 × 10 mm). The punched PDMS layer was bonded to the plain PDMS layer (as a top cover) using oxygen plasma treatment and punched again with six large circular holes (medium reservoirs, diameter = 8 mm) and two small circular holes (gel injection ports, diameter = 6 mm). Finally, the layer was bonded to a glass slide (bottom cover) using oxygen plasma treatment. The detailed procedure for fabricating a microfluidic device has been described in the previous study.[49,50] The chamber was pretreated with 2 mg mL^{-1} of dopamine hydrochloride (H8502, Sigma–Aldrich, United States) dissolved in 10 mM Tris-HCl buffer (pH 8.5, TR2016-050-85, Biosesang, South Korea) for 3 h to avoid detaching the cell-mixed gel from the PDMS wall. Following the aspiration of the dopamine solution, the chamber was rinsed with phosphate-buffered saline (PBS, 17–516Q, Lonza, Switzerland) and stored in a refrigerator filled with PBS.

Cell Culture: Human brain microvascular endothelial cells (hBMECs, #1000, ScienCell, CA, United States) were cultured to 90% confluency in 0.1 mg mL^{-1} collagen type I-coated T75 flasks using an endothelial cell culture media kit (ECM, #1001, ScienCell) supplemented with 1% endothelial cell growth supplement (ECGS, #1052, ScienCell), 1% penicillin/streptomycin (P/S, #0503, ScienCell), and 5% fetal bovine serum (FBS, #0025, ScienCell). The hBMECs were subcultured using 0.05% trypsin/EDTA (T/E, 25 200 056, Gibco, United States; 1/5 dilution of 0.25% T/E in Dulbecco's PBS [DPBS, BE17-512Q, Lonza]), following the manufacturer's protocol.

The Immortalized Human Microglia–SV40 cell line (IMhu) was purchased from Applied Biological Material Inc. (T0251, Milton, Canada) and cultured in Dulbecco's modified Eagle medium and Ham's F-12 (DMEM-F12, 11320-033, Gibco, United States) supplemented with 10% (v/v) fetal bovine serum (Corning, United States) and 1% (v/v) P/S. The SV40 cells were subcultured using 0.25% T/E following the manufacturer's protocol.

ReN VM human neural progenitor cells (ReN cells, SCC008, Merck, United States) were cultured on Matrigel-coated T75 flasks in proliferation media; DMEM-F12 (1:1, 11320-033, Gibco, United States) supplemented with 1% penicillin-streptomycin-amphotericin B mix (P/S/A, 17–745E, Lonza, Switzerland), 2% B27 (17504-044, Gibco), 2 µg mL^{-1} of heparin (H3149, Sigma–Aldrich), 5 µM of forskolin (F3917, Sigma–Aldrich), 20 ng mL^{-1} of epidermal growth factor (EGF, GF144,

© 2022 The Authors. Advanced Functional Materials published by Wiley-VCH GmbH

Merck, United States), and 20 ng mL^{-1} fibroblast growth factor (bFGF, GF003, Merck). The ReN cells were subcultured using Accutase cell detachment solution (SCR005, Merck) following the manufacturer's protocol. They were then differentiated in differentiation media and proliferation media without EGF and bFGF. The media was changed every 2–3 days.

Hydrogel Preparation for 3D Cell Culture: The hydrogel was composed of collagen type I for structural support and Matrigel and laminin for the differentiation of ReN cells to neurons. Collagen type I (Rat tail, 354 249, Corning, United States) was prepared by adding 10X DMEM (D2554, Sigma–Aldrich, Unites States) and 1 *N* sodium hydroxide (NaOH, S2770, Sigma–Aldrich) to rat tail collagen stock (Corning) to a final concentration of 5 mg mL^{-1} according to the manufacturer's instructions. Finally, collagen type I (5 mg mL^{-1}) was mixed with Matrigel (356 234, Corning) and laminin (1–2 mg mL^{-1}, L2020, Sigma–Aldrich) at a ratio of 6:3:1.

Construction of In Vitro Vasculature within the Cell-Embedded Hydrogel: SV40 and ReN cells were embedded in the optimized hydrogel at a density of 4×10^4 and 4×10^6 cell mL^{-1}, respectively, considering the proliferation rate (doubling time: 48–52 h) of SV40 and in vivo ratio of microglia to neurons.[51,52] The cell-embedded gel was injected into a chamber containing microneedles (outer diameter = 235 µm) and incubated at 37 °C for 30 min. The microneedles were removed from the gel, and 30 µL of the hBMEC suspension (2×10^6 cells mL^{-1}) was infused on the inner surface of the channel. After incubating for 10 min, the non-adherent endothelial cells were washed out.

Preparation of DEPs: The DEPs (SRM2975) were purchased from the National Institute of Standard Technology (United States). The DEP stock solution was dissolved in PBS at a concentration of 10 mg mL^{-1} and sonicated for 1 h. Before the experiment, the DEP stock solution was vortexed for 3 min, sonicated for 30 min, and immediately diluted in the cell culture medium at a concentration of 200 µg mL^{-1}.

Characterization of DEPs and PM2.5: A clear image of the DEPs was obtained using a scanning electron microscope (SEM; Nova Nano SEM 200, FEI company, United States). DEP powder was attached to carbon tapes on aluminum. SEM images were acquired by controlling the magnification at 10 kV. The size distribution and zeta potential of the DEPs were analyzed using zeta-potential and dynamic light scattering (DLS) particle size analyzer (ELSZ-1000, Otsuka Electronics, Japan). The DEP components were analyzed using a high-resolution field emission SEM (FE-SEM, Inspect F50, FEI company, United States) and an energy-dispersive X-ray spectroscopy (EDS) system.

Stimulation of the Human NGV Model by DEPs: When the brain blood vessel matured, the DEPs were diluted in the cell culture medium at a concentration of 200 µg mL^{-1}. DEP-enriched medium was infused into the endothelium through gravity-driven flow and incubated at 37 °C for 24 h. The DEP rapidly adhered to the blood vessel and the absorption level reached to saturation level in 24 h. To avoid excessive exposure, the medium was then replaced with a fresh cell culture medium.

Measurement and Estimation of Vascular Permeability: Fluorescein isothiocyanate (FITC)-dextran (40 kDa; FD40, Sigma–Aldrich) was used to quantify the permeability of the engineered brain endothelium with 10 µM (diluted in PBS). The medium was aspirated from each reservoir, and the FITC-dextran solution was infused into the endothelium. The solution filled the channel and diffused through the intercellular gap into the collagen scaffold. Molecular transport was monitored by capturing the sequential fluorescence using a Zeiss LSM700 confocal laser scanning microscope (CLSM; Zeiss, Oberkochen, Germany). Fluorescence images were acquired at 1 min intervals for 5 min and analyzed using MATLAB (MathWorks, MA, United States). Vascular permeability was quantified using the mean fluorescence intensity on both sides of the channel and its variation at different time intervals, as previously reported.[49,53]

Two fluorescence-labeled nanoparticles with different size (SPHEROTM Fluorescent Particles Polystyrene (0.04–0.06 µm), Purple/ 1.0% w/v (Cat. FP-00562-2) and SPHEROTM Fluorescent Particles Polystyrene (0.1–0.3 µm), Purple/ 1.0% w/v (Cat. FP-0262-2), Spherotech, Inc., United States) were used to analyzed particle transportation through engineered brain endothelium.

Analysis of Cell Viability: The viability staining solution was prepared by mixing Calcein-AM (C1430; Invitrogen, Carlsbad, CA, United States), propidium iodide (PI; P4564; Sigma–Aldrich), and Hoechst 33 342 (H3570; Invitrogen) in serum-free medium at concentrations of 1 µM, 1 and 10 µg mL^{-1}, respectively. To evaluate the survival of the cells exposed to DEPs, the chips were incubated with the staining solution for 30 min. The chips were then washed with fresh media. Fluorescent images of the live and dead cells on the chips were acquired using a Zeiss LSM700 CLSM, and cell viability was quantified by counting the number of live cells (green) and total cells (blue). Cell viability in GM-CSF- and antibody-treated conditions (in Figure 5) was analyzed using the cell proliferation WST-1 reagent (Roche, Switzerland). Cell-embedded gels were isolated from the NGV chips and incubated in WST-1 solution for 40 min according to the manufacturer's protocols. After incubation, the absorbance was measured at 450 nm using a Synergy HTX Multi-Mode Microplate Reader (BioTek, United States), and then, the cell viability was calculated.

Antibodies: Anti-CD31 (PECAM-1, sc-376764, Santa Cruz, United States), anti-VE-cadherin (sc-9989, Santa Cruz), anti-ZO-1 (33-9100, Invitrogen), anti-Occludin (sc-133256, Santa Cruz), anti-ICAM-1 (sc-390483, Santa Cruz), anti-GFAP (G3893, Sigma–Aldrich), anti-vimentin (sc6260, Santa Cruz), anti-p-tau Ser202Thr205 (AT8, MN1020, Invitrogen), anti-tau (sc-166060, Santa Cruz), anti-β-amyloid (8243, Cell Signaling, United States), anti-MAP2 (ab5392, Abcam, United Kingdom), Anti-Tuj1 (ab52623, Abcam), anti-iNOS (PA1-036, Invitrogen), anti-NF-kB (sc-8008, Santa Cruz), anti-CD11b (ab133357, Abcam, United Kingdom), anti-CD40 (ab13545, Abcam), and anti-CD68 (sc20060, Santa Cruz) antibodies were used for immunofluorescence staining and immunoblotting. Anti-β-actin (sc-47778, Santa Cruz), anti-GAPDH (sc-47724, Santa Cruz), anti-lamin A/C (sc-7292, Santa Cruz), anti-β-tubulin (sc-5274, Santa Cruz), and horseradish peroxidase (HRP)-linked anti-rabbit IgG (7074, Cell Signaling), and HRP-linked anti-mouse IgG (7076, Cell Signaling) antibodies were used for western blotting. Phalloidin tetramethylrhodamine B isothiocyanate (Phalloidin-TRITC, P1951, Sigma–Aldrich), 4′,6-diamidino-2-phenylindole (DAPI, D9564, Sigma–Aldrich), Alexa Fluor 488 goat anti-mouse IgG (A-11001, Invitrogen), Alexa Fluor 594 goat anti-rabbit IgG (A-11012, Invitrogen), and Alexa Fluor 647 goat anti-chicken IgG (A-21449, Invitrogen) were used for immunofluorescence staining.

Inhibition of Microglia Activation: Pioglitazone (30 µM, Sigma–Aldrich), minocycline (30 µM, Sigma–Aldrich), and astaxanthin (30 µM, Sigma–Aldrich) were used to inhibit microglial activation.

Analysis of the Effect of GM-CSF on the NGV Model: Human GM-CSF antibody (AF-215-NA, R&D System, United States) and recombinant human GM-CSF protein (215-GM-010/CF, R&D System) were used to study the effects of GM-CSF on microglial activation and neurodysfunction or degeneration. GM-CSF (5 ng mL^{-1}) was used to treat microglia mono-cultured and NGV models. To neutralize the action of GM-CSF, 1 µg mL^{-1} of GM-CSF antibody was added to the NGV model for 48 h.

Immunofluorescence Staining: To stain the cells cultured on the chip, the chips were fixed with 4% (v/v) paraformaldehyde for 30 min at 25 °C. After the chips had been washed twice with PBS, they were permeabilized with 0.3% (v/v) Triton X-100 (Sigma–Aldrich) and 3% (w/v) bovine serum albumin (BSA; Sigma–Aldrich) in PBS for 1 h. The chips were then incubated with primary antibodies diluted in 3% (w/v) BSA solution at the recommended concentration overnight at 4 °C. Following incubation, the chips were washed three times with PBS and incubated with secondary antibodies diluted in 3% (w/v) BSA solution at room temperature for 2 h. To stain the nuclei, the cells were treated with DAPI for 30 min at room temperature. Fluorescent z-stack images were acquired using a Zeiss LSM700 CLSM.

Western Blot: The PDMS cover of the ECM chamber on the device was removed using a blade cutter. The cell-embedded gels were then isolated from the NGV chips. The total proteins of the cells in the NGV chip were extracted using RIPA cell lysis buffer (1×, R4200, GenDepot, United States) supplemented with Halt Protease and Phosphatase Inhibitor Cocktail (78 440, Thermo Scientific, United States). Nucleus

© 2022 The Authors. Advanced Functional Materials published by Wiley-VCH GmbH

16163028, 0, Downloaded from https://onlinelibrary.wiley.com/doi/10.1002/adfm.202210123 by Seoul National University, Wiley Online Library on [29/12/2022]. See the Terms and Conditions (https://onlinelibrary.wiley.com/terms-and-conditions) on Wiley Online Library for rules of use; OA articles are governed by the applicable Creative Commons License

and cytoplasmic fractionation were performed using NE-PER Nuclear and Cytoplasmic Extraction Reagents (78 833, Thermo Scientific) following the manufacturer's instructions. The concentrations of extracted proteins were measured using the Bradford assay (Bio-Rad Protein assay dye reagent concentrate, United States). In brief, 10 µg of protein were subjected to sodium dodecyl sulfate-polyacrylamide gel electrophoresis and transferred to a NitroPure Nitrocellulose transfer membrane (LC7033-300, GenDepot) for blotting. Primary antibodies and HRP-conjugated secondary antibodies were used to label target proteins. Protein expression was detected using West-Q Pico Dura ECL solution (W3653, GenDepot, United States), and the membranes were imaged using the iBright CL750 Imaging System (A44116, Invitrogen).

Cytokine Level Analysis: The production of IL-6 and IL-8 was quantified using the Human IL-6 Quantikine ELISA Kit and Human IL-8/CXCL8 Quantikine ELISA Kit (R&D Systems, United States) according to the manufacturer's protocol. Cytokine profiles were analyzed using a human cytokine antibody array (ab133997, Abcam) according to the manufacturer's protocol. The array membrane was shown in Figure S4 (Supporting Information). The cell culture supernatant was collected from the chips on days 9 (200 µL per chip, DEP exposure: 24 h) and 11 (400 µL per chip, DEP exposure: 72 h) and centrifuged to remove visible PM.

Detection of Oxidative Modification of Proteins: The oxidative modification of proteins (introduction of carbonyl groups into protein side chains) was detected using an OxyBlot Protein Oxidation Detection Kit (S7150, Sigma–Aldrich). First, cell-embedded hydrogel scaffolds were isolated from the chips and homogenized using a Dounce Tissue Grinder (20–30 passes) with a final concentration of 0.1% protease inhibitor cocktail in RIPA buffer (R0278, Sigma–Aldrich). Cell debris and the gel were removed by centrifugation at 16000 rpm for 20 min. Protein concentrations were determined using the Bradford protein assay. Protein samples were prepared by diluting the lysate with RIPA buffer to a final concentration of 3 µg μL^{-1}.

Measurement of H_2O_2 Production: The production of H_2O_2 was measured using a hydrogen peroxide assay kit (ab102500, Abcam). Cell culture supernatants were collected from the chips on day 9 (200 µL per chip, DEP exposure: 24 h) and day 11 (400 µL per chip, DEP exposure: 72 h). The cell-embedded hydrogel scaffolds were harvested to further molecular study. The cell-embedded gels were homogenized using a Dounce Tissue Grinder (20–30 passes) with the assay buffer. The cells and fluid samples were centrifuged, and the supernatants were transferred to clean tubes. The samples were deproteinized by the addition of perchloric acid (PCA) and potassium hydroxide (KOH). The H_2O_2 concentration was verified by reacting the samples with OxiRed Probe and HRP and detecting the absorbance using a microplate reader. All experiments were performed on ice following the manufacturer's instructions.

Calcium Imaging of Neurons: A concentrated stock solution of calcium detection probe was prepared by dissolving 50 µg of Fluo4-AM (F10489, Invitrogen) in 50 µL of 20% (w/v) Pluronic F-127 (Sigma–Aldrich) in dimethyl sulfoxide (Sigma–Aldrich). The chips were then incubated with a probe solution diluted in calcium-free warm PBS at 1:1000 for 30 min. A fluorescent image of the neuronal calcium signal was captured at 2-s intervals using a Zeiss LSM700 CLSM. The value of F/F_0 was calculated based on the fluorescence intensity extracted using Java-based image processing program (ImageJ, NIH, United States) and visualized as a heatmap.

Detection of ROS Production: To detect ROS in the cells, a 2′,7′-dichlorofluorescein diacetate (DCFDA/H2DCFDA)-cellular ROS detection assay kit (ab113851, Abcam), which was a cell-permeant oxidation sensing indicator, was used according to the manufacturer's protocol. In brief, 20 µM of DCFDA solution was diluted in cell culture medium and treated with the NGV chip for 1 h. The intracellular ROS production was visualized using a Zeiss LSM700 CLSM.

Quantitative Analysis of Fluorescence and Blotting Images: The band intensity from western blotting and fluorescence intensity of immunofluorescence images were quantified by using ImageJ software. For analysis of western blotting results, band signals were normalized to each loading control signal. For a better comparison, the normalized values were calculated as fold changes based on the control. All quantification results are shown in Figure S7 (Supporting Information), below or next to the blotting image. The fluorescence images captured at the same laser intensity were analyzed using ImageJ for image-based analysis. The relative fluorescence intensity was also normalized as fold changes based on the control.

Statistical Analysis: Prism ver. 9 (GraphPad, United States) was used for the statistical analyses. Statistical comparisons between two experimental groups were performed using the unpaired two-tailed *t*-tests. Comparisons among more than three groups were performed using a one-way analysis of variance (ANOVA) with Tukey's multiple comparisons test. Box and whiskers plots represent the median (horizontal bars), 25 to 75 percentiles (box edges), and minimum to maximum values (whiskers) with all points. The scatter dot plot represents the mean ± SD with bars and error bars for all points. All experiments were performed in more than triplicates, and the number of experimental values and statistical methods were specified in each figure legend. *P*-values were represented with asterisks (*) are as follows: $*p < 0.05$; $**p < 0.01$; $***p < 0.001$; $****p < 0.0001$. All experiments were performed in triplicates, and the number of experimental values and statistical methods were specified in the caption of each figure.

Supporting Information

Supporting Information is available from the Wiley Online Library or from the author.

Acknowledgements

This work was supported by the National Research Foundation of Korea (NRF) grant funded by the Korean Government (MSIT; 2021R1A2B5B02086828, 2021R1C1C2005684, 2022M3A9B6018217, and 2022M3A9B6082678). This work was also supported by the Hongik University Research Fund. This work was supported by a grant of Korea Health Technology R&D Project through the Korea Health Industry Development Institute (KHIDI), funded by the Ministry of Health & Welfare, Republic of Korea (HI22C139400). This work was also supported by the Technology Innovation Program (20018522) funded by the Ministry of Trade, Industry & Energy (MOTIE), Republic of Korea.

Conflict of Interest

The authors declare no conflict of interest.

Author Contributions

S.S. and M.J. contributed equally to this work. S.S., M.J., H.K., and H.N.K. designed the experiments. S.S., M.J., and H.K. performed experiments and analyzed the data. N.C. provided MATLAB code for analyzing data. J.H.S., N.C., K.L., and H.N.K. supervised the overall study. All authors wrote, discussed the results and reviewed the manuscript.

Data Availability Statement

The data that support the findings of this study are available on request from the corresponding author. The data are not publicly available due to privacy or ethical restrictions.

© 2022 The Authors. Advanced Functional Materials published by Wiley-VCH GmbH

16163028, 0, Downloaded from https://onlinelibrary.wiley.com/doi/10.1002/adfm.202210123 by Seoul National University, Wiley Online Library on [29/12/2022]. See the Terms and Conditions (https://onlinelibrary.wiley.com/terms-and-conditions) on Wiley Online Library for rules of use; OA articles are governed by the applicable Creative Commons License

Keywords

blood–brain barriers, brain endothelial cells, diesel exhaust particles, granulocyte-macrophage colony-stimulating factor, neurodegeneration

Received: August 31, 2022
Revised: December 4, 2022
Published online:

[1] X. Li, L. Jin, H. Kan, *Nature* **2019**, *570*, 437.
[2] *Cent Eur J Public Health* **2014**, *22*, 53.
[3] R. Ko, M. Hayashi, M. Tanaka, T. Okuda, C. Nishita-Hara, H. Ozaki, E. Uchio, *Sci. Rep.* **2021**, *11*, 3417.
[4] S. G. Al-Kindi, R. D. Brook, S. Biswal, S. Rajagopalan, *Nat. Rev. Cardiol.* **2020**, *17*, 656.
[5] R. S. Gangwar, G. H. Bevan, R. Palanivel, L. Das, S. Rajagopalan, *Redox Biol.* **2020**, *34*, 101545.
[6] D. E. Schraufnagel, *Exp. Mol. Med.* **2020**, *52*, 311.
[7] L. Peeples, *Proc Natl Acad Sci U S A* **2020**, *117*, 13856.
[8] R. You, Y. S. Ho, R. C. Chang, *J Biomed Sci* **2022**, *29*, 15.
[9] B. A. Maher, I. A. Ahmed, V. Karloukovski, D. A. MacLaren, P. G. Foulds, D. Allsop, D. M. Mann, R. Torres-Jardon, L. Calderon-Garciduenas, *Proc Natl Acad Sci U S A* **2016**, *113*, 10797.
[10] R. Peters, N. Ee, J. Peters, A. Booth, I. Mudway, K. J. Anstey, *J Alzheimers Dis* **2019**, *70*, S145.
[11] Z. J. Rhinehart, E. Kinnee, U. R. Essien, M. Saul, E. Guhl, J. E. Clougherty, J. W. Magnani, *JAMA Netw Open* **2020**, *3*, e2011760.
[12] I. Y. Hwang, D. Choi, J. A. Kim, S. Choi, J. Chang, A. J. Goo, A. Ko, G. Lee, K. H. Kim, J. S. Son, S. M. Park, *Sci. Rep.* **2022**, *12*, 8471.
[13] S. Antonsen, P. L. H. Mok, R. T. Webb, P. B. Mortensen, J. J. McGrath, E. Agerbo, J. Brandt, C. Geels, J. H. Christensen, C. B. Pedersen, *Lancet Planet Health* **2020**, *4*, e64.
[14] S. Seo, J. E. Lee, K. Lee, H. N. Kim, *Environ. Sci.: Nano* **2022**, *9*, 454.
[15] C. McKee, G. R. Chaudhry, *Colloids Surf B Biointerfaces* **2017**, *159*, 62.
[16] M. Kapalczynska, T. Kolenda, W. Przybyla, M. Zajaczkowska, A. Teresiak, V. Filas, M. Ibbs, R. Blizniak, L. Luczewski, K. Lamperska, *Arch. Med. Sci.* **2018**, *14*, 910.
[17] T. Hartung, *Parkinsonism Relat. Disord.* **2008**, *14*, S81.
[18] M. Jucker, *Nat. Med.* **2010**, *16*, 1210.
[19] G. A. Van Norman, *JACC Basic Transl Sci* **2019**, *4*, 845.
[20] E. Underwood, *Science* **2017**, *355*, 342.
[21] D. E. Ingber, *Nat. Rev. Genet.* **2022**, *23*, 467.
[22] G. D. Leikauf, S. H. Kim, A. S. Jang, *Exp. Mol. Med.* **2020**, *52*, 329.
[23] D. Huh, B. D. Matthews, A. Mammoto, M. Montoya-Zavala, H. Y. Hsin, D. E. Ingber, *Science* **2010**, *328*, 1662.
[24] Y. Li, Y. Liu, C. Hu, Q. Chang, Q. Deng, X. Yang, Y. Wu, *Environ Int* **2020**, *143*, 105598.
[25] Y. J. Kang, H. Y. Tan, C. Y. Lee, H. Cho, *Adv. Sci.* **2021**, *8*, 2101251.
[26] S. Seo, H. Kim, J. H. Sung, N. Choi, K. Lee, H. N. Kim, *Biomaterials* **2020**, *232*, 119732.
[27] M. L. Block, X. Wu, Z. Pei, G. Li, T. Wang, L. Qin, B. Wilson, J. Yang, J. S. Hong, B. Veronesi, *FASEB J.* **2004**, *18*, 1618.
[28] J. A. Kim, H. N. Kim, S. K. Im, S. Chung, J. Y. Kang, N. Choi, *Biomicrofluidics* **2015**, *9*, 024115.
[29] K. D. A. Rienecker, R. G. Poston, R. N. Saha, *ASN Neuro* **2020**, *12*, 175909142097480.
[30] G. R. Frost, Y. M. Li, *Open Biol* **2017**, 7.
[31] C. Lerdkrai, N. Asavapanumas, B. Brawek, Y. Kovalchuk, N. Mojtahedi, M. Olmedillas Del Moral, O. Garaschuk, *Proc Natl Acad Sci U S A* **2018**, *115*, E1279.
[32] A. M. Jurga, M. Paleczna, K. Z. Kuter, *Front Cell Neurosci* **2020**, *14*, 198.
[33] V. Cipollini, F. Troili, F. Giubilei, *Int. J. Mol. Sci.* **2019**, *20*, 2812.
[34] S. Bachiller, I. Jimenez-Ferrer, A. Paulus, Y. Yang, M. Swanberg, T. Deierborg, A. Boza-Serrano, *Front. Cell Neurosci.* **2018**, *12*, 488.
[35] F. Leng, P. Edison, *Nat. Rev. Neurol.* **2021**, *17*, 157.
[36] H. Chun, H. Im, Y. J. Kang, Y. Kim, J. H. Shin, W. Won, J. Lim, Y. Ju, Y. M. Park, S. Kim, S. E. Lee, J. Lee, J. Woo, Y. Hwang, H. Cho, S. Jo, J. H. Park, D. Kim, D. Y. Kim, J. S. Seo, B. J. Gwag, Y. S. Kim, K. D. Park, B. K. Kaang, H. Cho, H. Ryu, C. J. Lee, *Nat. Neurosci.* **2020**, *23*, 1555.
[37] D. S. A. Simpson, P. L. Oliver, *Antioxidants (Basel)* **2020**, *9*, 9080743.
[38] Q. Zhao, X. Wu, S. Yan, X. Xie, Y. Fan, J. Zhang, C. Peng, Z. You, *J Neuroinflammation* **2016**, *13*, 259.
[39] M. M. F. Machado, T. B. Bassani, V. Coppola-Segovia, E. L. R. Moura, S. M. Zanata, R. Andreatini, M. Vital, *Pharmacol. Rep.* **2019**, *71*, 556.
[40] K. Kobayashi, S. Imagama, T. Ohgomori, K. Hirano, K. Uchimura, K. Sakamoto, A. Hirakawa, H. Takeuchi, A. Suzumura, N. Ishiguro, K. Kadomatsu, *Cell Death Dis.* **2013**, *4*, e525.
[41] X. Zhou, J. Zhang, Y. Li, L. Cui, K. Wu, H. Luo, *Life Sci.* **2021**, *267*, 118943.
[42] H. O. Dikmen, M. Hemmerich, A. Lewen, J. O. Hollnagel, B. Chausse, O. Kann, *J Neuroinflammation* **2020**, *17*, 235.
[43] R. E. Gonzalez-Reyes, M. O. Nava-Mesa, K. Vargas-Sanchez, D. Ariza-Salamanca, L. Mora-Munoz, *Front Mol Neurosci* **2017**, *10*, 427.
[44] S. F. Carter, K. Herholz, P. Rosa-Neto, L. Pellerin, A. Nordberg, E. R. Zimmer, *Trends Mol. Med.* **2019**, *25*, 77.
[45] N. Korte, R. Nortley, D. Attwell, *Acta Neuropathol.* **2020**, *140*, 793.
[46] A. P. Sagare, R. D. Bell, Z. Zhao, Q. Ma, E. A. Winkler, A. Ramanathan, B. V. Zlokovic, *Nat. Commun.* **2013**, *4*, 2932.
[47] J. Wang, B. J. Gu, C. L. Masters, Y. J. Wang, *Nat. Rev. Neurol.* **2017**, *13*, 612.
[48] J. M. Tarasoff-Conway, R. O. Carare, R. S. Osorio, L. Glodzik, T. Butler, E. Fieremans, L. Axel, H. Rusinek, C. Nicholson, B. V. Zlokovic, B. Frangione, K. Blennow, J. Menard, H. Zetterberg, T. Wisniewski, M. J. de Leon, *Nat. Rev. Neurol.* **2015**, *11*, 457.
[49] S. Seo, C. H. Choi, K. S. Yi, S. U. Kim, K. Lee, N. Choi, H. J. Lee, S. H. Cha, H. N. Kim, *Biofabrication* **2021**, *13*, 035039.
[50] S. Seo, S.-Y. Nah, K. Lee, N. Choi, H. N. Kim, *Adv. Funct. Mater.* **2022**, *32*, 2106860.
[51] S. D. Skaper, *CNS Neurol Disord Drug Targets* **2011**, *10*, 44.
[52] J. L. Frost, D. P. Schafer, *Trends Cell Biol.* **2016**, *26*, 587.
[53] S. Seo, S. Y. Nah, K. Lee, N. Choi, H. N. Kim, *Adv. Funct. Mater.* **2022**, *32*, 2106860.

© 2022 The Authors. Advanced Functional Materials published by Wiley-VCH GmbH

16163028, 0, Downloaded from https://onlinelibrary.wiley.com/doi/10.1002/adfm.202210123 by Seoul National University, Wiley Online Library on [29/12/2022]. See the Terms and Conditions (https://onlinelibrary.wiley.com/terms-and-conditions) on Wiley Online Library for rules of use; OA articles are governed by the applicable Creative Commons License